Journal of Materials Chemistry A

ROYAL SOCIETY OF CHEMISTRY

PAPER

View Article Online
View Journal | View Issue

Cite this: J. Mater. Chem. A, 2023, 11, 6530

Activation in the rate of oxygen release of $Sr_{0.8}Ca_{0.2}FeO_{3-\delta}$ through removal of secondary surface species with thermal treatment in a CO_2-free atmosphere†

Giancarlo Luongo, Alexander H. Bork, Paula M. Abdala, Yi-Hsuan Wu, Evgenia Kountoupi, Felix Donat * and Christoph R. Müller *

We elucidate the underlying cause of a commonly observed increase in the rate of oxygen release of an oxygen carrier with redox cycling (here specifically for the perovskite $Sr_{0.8}Ca_{0.2}FeO_{3-\delta}$) in chemical looping applications. This phenomenon is often referred to as activation. To this end we probe the evolution of the structure and surface elemental composition of the oxygen carrier with redox cycling by both textural and morphological characterization techniques (N_2 physisorption, microscopy, X-ray powder diffraction and X-ray absorption spectroscopy). We observe no appreciable changes in the surface area, pore volume and morphology of the sample during the activation period. X-ray powder diffraction and X-ray absorption spectroscopy analysis (at the Fe and Sr *K*-edges) of the material before and after redox cycles do not show significant differences, implying that the bulk (average and local) structure of the perovskite is largely unaltered upon cycling. The analysis of the surface of the perovskite *via* X-ray photoelectron and *in situ* Raman spectroscopy indicates the presence of surface carbonate species in the as-synthesized sample (due to its exposure to air). Yet, such surface carbonates are absent in the activated material, pointing to the removal of carbonates during cycling (in a CO_2-free atmosphere) as the underlying cause behind activation. Importantly, after activation and a re-exposure to CO_2, surface carbonates re-form and yield a deactivation of the perovskite oxygen carrier, which is often overlooked when using such materials at relatively low temperature (≤500 °C) in chemical looping.

Received 22nd November 2022
Accepted 26th February 2023

DOI: 10.1039/d2ta09102j

rsc.li/materials-a

1. Introduction

Perovskite-based oxides find application in many areas, including solid oxide fuel cells,[1,2] catalysis,[3,4] gas separation membranes,[5,6] photoelectrochemical water splitting,[7,8] and as oxygen carriers for chemical looping applications.[3,9,10] Perovskite oxides have the general formula $ABO_{3-\delta}$, where the A cation is a rare or alkaline earth metal, the B cation is a transition metal oxide and delta δ refers to the oxygen non-stoichiometry.[3] Perovskites possess high mixed ionic and electronic conductivity, as well as high rates of oxygen exchange with molecular oxygen in the gas phase.[11,12] Chemical looping applications exploit the reversible release and uptake of oxygen from perovskites according to eqn (1):[9]

$$ABO_{3(s)} \leftrightarrow ABO_{3-\delta(s)} + \frac{\delta}{2}O_{2(g)} \quad (1)$$

At a given temperature, T, some perovskites release gaseous oxygen in a N_2 atmosphere (or in other low oxygen partial pressure, pO_2, environments) and can be re-oxidized in air (high pO_2). Perovskites can accommodate a wide variety of A- and B-site cations, which allows for the tuning of their chemical and physical properties (*e.g.* temperature and quantity of oxygen release, enthalpy of reaction, and melting temperature).[9,13] Specifically, strontium and iron-based perovskites were identified as promising oxygen carriers for low temperature chemical looping applications (400–600 °C).[9,11,14] Several works studied the effect of the substitution of Sr- and/or Fe-with different cations in $SrFeO_{3-\delta}$ (*e.g.* La or Ca for the A-site, or Co, Ni or Cu for the B-site) on its thermodynamic properties (*e.g.* the equilibrium oxygen partial pressure, enthalpy of reaction or oxygen storage capacity), which largely determine the suitability of an oxygen carrier for a given chemical looping application.[9,12] We investigated in a previous work the effect of Ca A- or Co B-site substitution on the performance of these materials (*i.e.* $Sr_{1-x}Ca_xFeO_{3-\delta}$ and $SrFe_{1-x}Co_xO_{3-\delta}$) for chemical looping air separation (CLAS). When assessing the redox cyclic stability of both unsubstituted and substituted samples, we observed that the amount of oxygen released at 500 °C increased with the number

Laboratory of Energy Science and Engineering, Department of Mechanical and Process Engineering, ETH Zurich, Leonhardstrasse 21, 8092 Zürich, Switzerland. E-mail: donatf@ethz.ch; muelchri@ethz.ch

† Electronic supplementary information (ESI) available. See DOI: https://doi.org/10.1039/d2ta09102j

of redox cycles, indicating that the material "activated" during redox cycling.[14]

A cycle number-dependent activation of oxygen carriers in chemical looping applications is not specific to the $SrFeO_{3-\delta}$ family, and has indeed been reported for many other oxides, including natural minerals such as ilmenite and supported Fe- or Cu-based oxides.[15–17] Most of these studies have investigated the material behavior at high temperatures (>800 °C).[18–20] For example, for ilmenite, a type of oxygen carrier that has been used for chemical looping-based combustion processes, it was found that long heat treatments (*e.g.* 950 °C for 24 h in air) enhance its redox activity.[21–23] With redox cycling, ilmenite was found to activate further[24,25] and there is a clear correlation between the degree of reduction and the extent of activation in each redox cycle.[26] The activation of ilmenite is accompanied by the formation of surface cracks and an increase in porosity, from ~1% up to ~40%,[27] but also the segregation of iron oxide from the Fe–Ti–O mixed phases and the lowering of the oxygen storage capacity (OSC).[28] Other routes of activation of oxygen carriers such as ilmenite include their doping, *e.g.* by K using K_2CO_3 as the precursor.[29–33] For Fe–O-based oxygen carriers, the interactions of Fe with the support material (often Al_2O_3) and the re-distribution of Fe within the material have been put forward to explain their activation, but also its deactivation, during redox cycling.[34–38]

Concerning perovskite-based oxygen carriers for chemical looping application at lower temperatures (≤500 °C), the phenomenon of activation has not been studied and hence the underlying cause is currently unknown. However, in other research areas, *e.g.* electrochemistry in the context of the oxygen reduction reaction (ORR) and the oxygen evolution reaction (OER), the activation and deactivation of perovskites have indeed been studied thoroughly. Different from chemical looping, here activation and deactivation refer to an increase and decrease, respectively, of the oxygen exchange rates and the catalytic activity of perovskites, without changes in the bulk phase.[39–42] For example, for the electrocatalyst (La, Sr)(Mn, Fe, Co)$O_{3-\delta}$ it was found that a decrease in the rate of oxygen exchange was accompanied by the segregation of the A-site cation Sr from the perovskite structure and the formation of secondary phases on the surface, identified as SrO_x or $SrCO_3$.[39,43–48] It was also shown that the deactivation could be reversed by thermal treatment at $T > 800$ °C.[39,40]

Hence, the aim of this work is to elucidate the prevailing activation mechanism of $Sr_{1-x}Ca_xFeO_{3-\delta}$ perovskites in low-temperature chemical looping applications. To this end, we perform a detailed (bulk) structural and morphological characterization of the material during activation. This is complemented by measurements of the material's surface and changes thereof using X-ray photoelectron spectroscopy (XPS) and *in situ* Raman spectroscopy. Our findings show that CO_2 (often present as impurity in both oxidizing and reducing gas streams) impair the performance of Sr-containing oxygen carriers through the formation of surface carbonates. Exposure to CO_2-free streams gradually removes these surface carbonates, leading in turn to an activation of the material. These findings are of relevance for both the design of oxygen carrier materials and their operation in low-temperature chemical looping process schemes.

2. Experimental

2.1 Synthesis of the oxygen carrier

The perovskites were synthesized *via* a sol–gel method by dissolving stoichiometric amounts of nitrate precursors, *i.e.* $Sr(NO_3)_2$ (Sigma Aldrich, ACS reagent, 99.9%), $Fe(NO_3)_3 \cdot 9H_2O$ (Sigma Aldrich, ACS reagent, ≥ 98%) and $Ca(NO_3)_2 \cdot 4H_2O$ (Sigma Aldrich, 99%) in deionized water together with citric acid (3 : 1 molar ratio of citric acid to metal ions) and ethylene glycol (1.2 : 1 molar ratio of ethylene glycol to citric acid). The solution was held at 80 °C until a gel formed and subsequently dried at 130 °C for 10 h. The powder was crushed and first calcined in air at 500 °C for 7 h (heating rate 3 °C min^{-1}) and then at 1000 °C for 10 h (heating rate 5 °C min^{-1}).

2.2 Characterization of the oxygen carrier

2.2.1 X-ray powder diffraction. Synchrotron X-ray diffractograms of the as prepared materials were collected at the ID31 beamline of the European Synchrotron Radiation Facility (ESRF), using a monochromatic beam, set at a wavelength of 0.1770 Å focused to a size of 0.6 mm × 0.6 mm, and a Pilatus3 X CdTe 2M detector in a transmission geometry (Debye–Scherrer). The powder samples were loaded in 1 mm Kapton capillary tubes. The azimuthal parameters and the sample-to-detector distance (~84 cm) were obtained using a CeO_2 diffraction standard. The software PyFAI was used for the azimuthal integration of the data. Laboratory based XRD patterns were collected in a PANalytical Empyrean diffractometer equipped with an X'Celerator Scientific ultra-fast line detector and Bragg–Brentano HD incident beam optics, using Cu $K_{\alpha 1,2}$ radiation (operated at 45 kV and 40 mA). A secondary monochromator was used to suppress unwanted fluorescence originating from iron in the samples. The scans were collected in the 2θ range of 10–100° with a step size of 0.022°, and the time of each measurement was 3 h. *In situ* XRD measurements were carried out in the same diffractometer equipped with an Anton Paar XRK 900 reactor chamber and using a Macor sample holder. First, the sample was heated up to 500 °C at 25 °C min^{-1} under a flow of air. This was followed by redox cycling using pure N_2 (200 mL min^{-1}) for reduction and air (200 mL min^{-1}) for re-oxidation. The scan time of each diffractogram over the 2θ range of 31°–34° was ~65 s. The software FullProf was used to analyze the XRD patterns, while the software WinPLOTR was used to analyze the evolution of the phase transition from perovskite to brownmillerite by fitting the 2θ position and intensity of the perovskite and brownmillerite peaks.[49] The cell parameter (a) of the cubic perovskite structure was calculated using Bragg's law and the plane d-spacing (eqn (2)) for a cubic system:

$$\frac{1}{d^2} = \frac{(h^2 + k^2 + l^2)}{a^2} \quad (2)$$

with $(hkl) = (110)$.[50]

2.2.2 Nitrogen physisorption. A Quantachrome NOVA 4000e N_2 adsorption analyzer was used to determine the surface area and the pore volume of the materials. Each sample was degassed at 250 °C for 2 h prior to the measurements. The Barret–Joyner–Halenda (BJH) model was used to calculate the pore volume of the materials.

2.2.3 Temperature-programmed desorption (TPD). TPD experiments were carried out in an AutoChem II 2920 connected to a mass spectrometer (MKS, Cirrus 2) for the instantaneous detection of gas species in very small concentrations. 70 mg of the as-synthesized oxygen carrier was loaded into a U-shape quartz reactor, heated to 700 °C (5 °C min^{-1}) in He (50 mL min^{-1}) or in 5% O_2/He (50 mL min^{-1}) and held for 30 min, before cooling down.

2.2.4 Electron microscopy. The morphology of the oxygen carrier was investigated using high resolution scanning electron microscopy (HR-SEM, FEI Quanta 200F).

2.2.5 X-ray photoelectron spectroscopy. XPS measurements were carried out by using a PHI Quantera SXM (ULVAC-PHI, Chanhassen, MN, USA), with a monochromatic Al K_α (1486.6 eV) source, using a beam diameter of 200 μm, and with the analyzer working in a constant-analyzer energy (CAE) mode. Survey spectra were acquired using the analyzer at a pass energy of 280 eV, a time step of 20 ms and a step size of 1.0 eV. High-resolution narrow scans were collected by using a pass energy of 55 eV and a step size of 0.1 eV. A low-voltage argon ion gun/electron neutralizer was used for all measurements. The binding energies were calibrated based on the C 1s spectrum at 284.6 eV and the fitting analysis was carried out by using the program CasaXPS (Casa Software Ltd). An indium-based substrate was used for the measurements, and background subtraction was performed following the Shirley method.[51] Air-tight XPS measurement was carried out by using a Sigma II instrument of Thermo Fisher Scientific, equipped with an UHV chamber, with non-monochromatic 200 W Al Kα source, a hemispherical analyzer, and a seven-channel electron multiplier. The analyzer-to-source and the emission angles were 50° and 0°, respectively. The survey and narrow scans used a pass energy of 25 eV. The measurement was carried out by using a custom-made air-tight cell to transfer the sample between the glovebox and the XPS instrument.

To estimate the atomic composition, the atomic sensitivity factors (ASF) of Scofield were used.[52] In the case of the Sr 3d spectrum, where different peaks originate from the same element due to orbital splitting, the following constraints were used: the difference in binding energy between the Sr $3d_{5/2}$ and Sr $3d_{3/2}$ components was 1.7 eV and the ratio between the peak areas of Sr $3d_{5/2}$ and Sr $3d_{3/2}$ was fixed at 1.5.[39]

2.2.6 X-ray absorption spectroscopy (XAS). XAS measurements were carried out at the Swiss-Norwegian beamline (BM31) at the European Synchrotron Radiation Facility (ESRF, Grenoble, France) at the Fe K-edge in transmission mode using a Si (111) double crystal monochromator. The samples were ground to fine powder, diluted with cellulose to optimize the transmission of X-rays, and then pelletized. The XAS data was processed using the Athena software (Demeter 0.9.20 software package).[53]

2.2.7 Raman spectroscopy. Raman spectroscopy measurements were performed on a DXR 2 Raman spectrometer (Thermo Fisher) using a 532 nm excitation laser with a spot size of ~2.1 μm at an optical magnification of 10×. All measurements were carried out in the range of 106–3500 cm^{-1} using a full range grating with a resolution of 1200 lines mm^{-1}. For each sample, at least five different areas of the sample were measured and averaged. *In situ* Raman spectroscopy measurements were conducted with the same instrument using a high temperature Linkam CCR1000 cell in which the sample was placed and exposed to N_2 or CO_2.

2.2.8 Thermogravimetric analyzer (TGA). The oxygen storage capacity (OSC), an indicator of the cyclic activity of the oxygen carrier, was determined using a Mettler Toledo TGA/DSC 3+. The total gas flow rate in all TG experiments was 200 mL min^{-1} (unless stated otherwise) and included a constant N_2 flow of 25 mL min^{-1} to purge the microbalance. In a typical experiment 30 mg of the sample (unless stated otherwise) was placed in a 70 μL alumina crucible, heated to 500 °C in compressed air at a rate of 25 °C min^{-1} and held for 60 min. During the isothermal period, redox cycles were performed by switching the gas atmosphere between pure N_2 (175 mL min^{-1}) and compressed air (175 mL min^{-1}). In experiments involving steam, the gas flowed through a small saturator (5 mL) filled with deionized water, resulting in a steam concentration of ~2% in the reaction chamber of the TGA. The measured OSC_m (in %) of the oxygen carrier was calculated using eqn (3), where m_{air} is the weight of the oxygen carrier at equilibrium in air and m_{N_2} is the weight of the oxygen carrier after changing the atmosphere to N_2.

$$OSC_m = \frac{m_{air} - m_{N_2}}{m_{air}} \cdot 100\ \% = \frac{\Delta m_s}{m_{air}} \cdot 100\ \% \quad (3)$$

The change in oxygen non-stoichiometry $\Delta\delta$, used to evaluate the relaxation time of the reaction, was calculated according to eqn (4):

$$\Delta\delta = \Delta m_s \cdot \frac{M_{OC}}{M_O} \quad (4)$$

where M_{OC} is the molar mass of the oxygen carrier and M_O the molar mass of oxygen.

3. Results and discussion

3.1 Activation in the rate of the oxygen release from $Sr_{1-x}Ca_xFeO_{3-\delta}$

The oxygen release and uptake of $Sr_{0.8}Ca_{0.2}FeO_{3-\delta}$ over ten redox cycles in a TGA at 500 °C is shown in Fig. 1a. Considering the first cycle, after 40 min of reduction in N_2 the OSC_m was 1.60 wt%. After a subsequent oxidation for 20 min in air, the mass had regained the initial value. In the following redox cycles, an increased mass loss was observed at the end of each consecutive reduction step, reaching an OSC_m of 2.15 wt% after the 10th reduction step. This is consistent with our previous results showing an increase in the rate of oxygen release, and hence the amount of oxygen released within a given time with

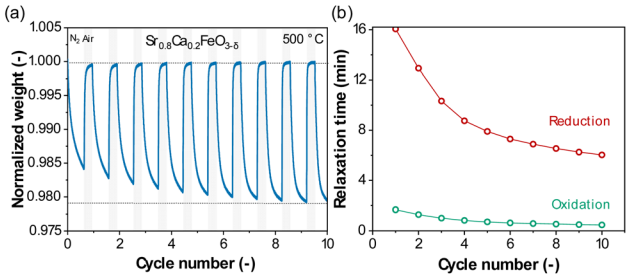

Fig. 1 (a) Normalized weight upon redox cycling (40 min reduction in N_2 and 20 min oxidation in compressed air) collected in the TGA at 500 °C for $Sr_{0.8}Ca_{0.2}FeO_{3-\delta}$; (b) relaxation times of the reduction and oxidation steps, obtained by fitting the temporal change of the normalized sample weight with an exponential decay function, as defined in eqn (5) and (6).

increasing cycle number.[14] The observed rates of the oxygen release and uptake can be quantified by fitting the change in the oxygen non-stoichiometry $\Delta\delta$ (eqn (4)) with an exponential first-order decay function,[54] as defined in eqn (5) and (6) for the reduction and oxidation steps, respectively:

$$\Delta\delta = a\cdot\left(1-e^{-\frac{t}{\tau_{RED}}}\right) \quad (5)$$

$$\Delta\delta = b\cdot\left(e^{-\frac{t}{\tau_{OX}}}\right) \quad (6)$$

Here, a and b are two fitting parameters, which could be interpreted, respectively, as the asymptotic value of the oxygen non-stoichiometry of the reduction reaction and the beginning of the oxidation reaction, only had the reaction time t approached infinity; since the reaction times were short in our cycling experiments and the reduction reaction incomplete, a and b were always different. τ_{RED} and τ_{OX} are the fitted relaxation times for the reduction and oxidation reactions (*e.g.* for the reduction step, after time $t = \tau_{RED}$, $\Delta\delta$ becomes $0.63 \times a$, meaning that the reaction has reached 63% of the fitted asymptotic value of the oxygen non-stoichiometry). In other words, a short relaxation time τ means that the asymptotic value of the oxygen non-stoichiometry for a given combination T and pO_2 is reached faster and the OSC_m is greater (in a given time) as opposed to a long relaxation time. Fig. S1† exemplary shows a fitting of the change in oxygen non-stoichiometry $\Delta\delta$ during reduction and oxidation in the first cycle of Fig. 1a using eqn (5) and (6). Fig. 1b plots the obtained relaxation times τ_{RED} and τ_{OX} over ten cycles, showing a clear decrease in τ_{RED} and τ_{OX} with cycle number. It is noteworthy that an activation occurred for both the reduction and oxidation steps, as evident by the decreasing values of the relaxation times for increasing cycle number, yet the degree of activation was significantly more pronounced in the reduction step. All fitted parameters (a, b, τ_{RED} and τ_{OX}) and goodness of fit (R^2) values obtained when calculating the relaxation times in Fig. 1b and 2 are provided in the ESI,† Table S1.

To elucidate the cause of the increase in the rate of oxygen release, first it is critical to examine under what operating conditions the phenomenon is observed and exclude any experimental artifacts. To this end, we investigated the influence of different sample compositions and operating conditions (*i.e.* atmosphere, particle size, flow rate, sample weight, temperature, and crucible type) on the activation behavior.

Fig. S2† shows the TGA curves obtained over ten redox cycles using $SrFeO_{3-\delta}$, $Sr_{0.9}Ca_{0.1}FeO_{3-\delta}$ and $Sr_{0.75}Ca_{0.25}FeO_{3-\delta}$ as the oxygen carriers.

We can observe an increase in the rate of oxygen release with increasing cycle number for all samples. Note that we studied only phase pure $Sr_{1-x}Ca_xFeO_{3-\delta}$ perovskites, hence the value of x is limited to $x \leq 0.25$, as reported in previous work.[14] Fig. S3† summarizes the effects of total flowrates, sample masses, particle size distributions, reducing atmospheres (by using also 5% H_2/N_2) and crucible sizes (a shallow 30 μL instead of a 70 μL crucible) on the activation behavior of $Sr_{0.8}Ca_{0.2}FeO_{3-\delta}$.

From these control experiments, we observed that each operating parameter affected the cyclic activation of $Sr_{0.8}Ca_{0.2}FeO_{3-\delta}$ to some degree (Fig. S3†), yet the phenomenon of activation was always observed. Hence, in the following a fixed set of experimental conditions was used (*i.e.* flow rate 200 mL min^{-1}, sample weight 30 mg, particle size 25–53 μm, 70 μL crucible).

In order to understand whether the activation of the perovskite is a temporary or long-lasting effect, we carried out "aging" experiments, in which the sample was cooled down after activation in the TGA and stored at ambient conditions in a closed vial for a fixed period of time. Fig. 3a summarizes the relaxation times as a function of the cycle number determined from cycling experiments (30 redox cycles each) for the as-synthesized sample and the same sample (redox-cycled) stored in the laboratory at ambient conditions for 1 week, another 2 weeks, another 2 h, and finally another 2 weeks again; the results of the individual redox cycling experiments are provided in Fig. S4.† From the first cycle to the thirtieth cycle we observed the expected activation behavior of the as-synthesized material described by a decrease in the relaxation time. After 1 week of storage in the laboratory, the sample displayed a longer relaxation time in the first cycle, *i.e.* the thirty-first cycle compared to the thirtieth cycle, which indicates that the sample deactivated during its storage at ambient conditions. From the subsequent storage and redox cycling experiments, we observed that a longer storage time (2 weeks compared to 2 h) resulted in a higher degree of deactivation (*i.e.* longer relaxation times). Hence, there was a direct correlation between the storage time and the degree of deactivation.

Since the perovskite deactivated in ambient conditions, we investigated whether the deactivation may be ascribed to humidity (H_2O) or CO_2 present in ambient air. For this purpose, we exposed the sample to dry CO_2 (1%, 5%, 10% CO_2/air) or H_2O (synthetic, CO_2-free, air with ~90% relative humidity) in the TGA (at 500 °C or 25 °C) for 20 min, between two sets of five redox cycles (Fig. 2). A slight, continuous weight gain was observed when exposing the sample to 2% H_2O at ambient temperature (Fig. 2d), which most likely can be ascribed to

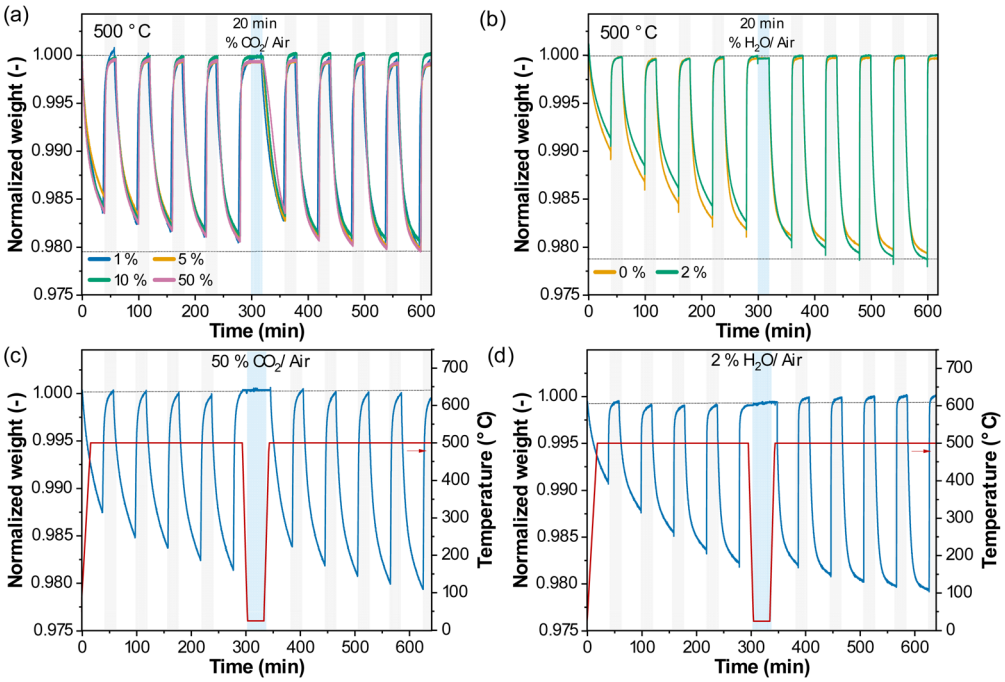

Fig. 2 Redox performance upon cycling with exposure to CO_2 or H_2O between two sets of 5 redox cycles at (a) and (b) 500 °C or (c) and (d) 25 °C. Normalized weight upon 5 redox cycles, followed by exposure (20 min) to (a) 1%, 5%, 10% or 50% CO_2/air, (b) 2% H_2O/air at 500 °C or (c) 50% CO_2/air, (d) 2% H_2O/air at 25 °C, and again 5 redox cycles at 500 °C.

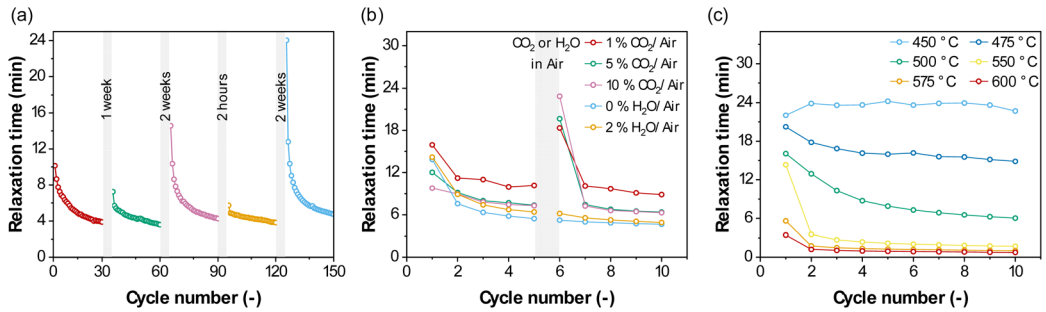

Fig. 3 Relaxation time of the reduction reaction as a function of cycle number. (a) Effect of laboratory storage under ambient conditions with the storage time being specified; (b) effect of exposure to a CO_2- or H_2O-rich atmosphere, for 20 min, between two sets of 5 redox cycles at 500 °C; (c) effect of temperature on the observed activation phenomenon.

adsorbed water. Such weight increase was not observed at 500 °C (Fig. 2b). Fig. 3b summarizes the relaxation times of the reduction reaction before and after the exposure to CO_2 or H_2O at 500 °C. The exposure to CO_2 resulted in a significantly increased relaxation time in the second set of the redox cycles, while the exposure to H_2O had no noticeable effect.

A similar observation was made after exposure to CO_2 at 25 °C, but there was no apparent effect on the rate of oxygen release after exposure to H_2O at 25 °C.

Therefore, we can conclude that the presence of CO_2 was the main cause of deactivation of the perovskite, while the effect of activation occurred through redox cycling in the absence of CO_2.

We note that the activation through redox cycling at 500 °C was gradual and incomplete after each of the 30 cycle experiments, *i.e.* the relaxation time was still decreasing after each of the 30 cycles as can be seen in Fig. 3a.

Fig. S5† shows TGA experiments carried out at 450 °C, 475 °C, 500 °C, 550 °C, 575 °C and 600 °C, with the corresponding relaxation times of the reduction steps as a function of cycle number summarized in Fig. 3c. The highest OSC of $Sr_{0.8}Ca_{0.2}FeO_{3-\delta}$ was achieved when operating at 500 °C and 550 °C (2.15 wt% and 2.08 wt%, respectively).[14] With increasing temperature, the rate of oxygen release increased, as evident by decreased relaxation times.

At the lowest temperature investigated, *i.e.* 450 °C, the relaxation time was 24 min and remained constant with cycle number, meaning that activation did not occur at this temperature, or at least was not observed within the time of reduction; this is discussed below in Section 3.4. At 475 °C, activation was

observed, and the relaxation time gradually decreased from 20 min in the first reduction step to 16 min in the 10th cycle. Increasing the reduction temperature further, we observed that the relaxation time stabilized after 6 cycles at 550 °C, 4 cycles at 575 °C and after 2 cycles at 600 °C. This suggests that the change of the material (in the structure or the surface, see the following sections) due to the presence of CO_2 occurred faster at higher temperatures, and that temperatures ≥475 °C were needed to activate the sample. In the following section, we investigated whether the observed activation/deactivation was related to structural changes in the bulk or the surface of the oxygen carrier.

3.2 Bulk perovskite structure and changes upon redox cycling

3.2.1 Ex-situ characterization before and after redox cycling. Fig. 4a shows the X-ray powder diffraction pattern of $Sr_{0.8}Ca_{0.2}FeO_{3-\delta}$. Previously,[14,55,56] a cubic structural model ($Pm\bar{3}m$) was used to describe the structure of $Sr_{0.8}Ca_{0.2}FeO_{3-\delta}$. However, our XRD measurements (using both synchrotron radiation and laboratory XRD at room temperature) revealed reflections that cannot be explained with a cubic structural model. We thus revised the crystal structure of this material by describing it with the orthorhombic *Cmmm* space group based on a previously reported structure,[57] and obtained the unit cell parameters $a = 10.9324(1)$ Å, $b = 7.7042(5)$ Å and $c = 5.4810(2)$ Å. The XRD patterns of $Sr_{0.8}Ca_{0.2}FeO_{3-\delta}$ collected in our laboratory before and after 30 redox cycles in the TGA are shown in Fig. 4b. The difference in the calculated cell parameters between the sample before and after cycling (Fig. S7†) is <0.05%, and we thus conclude that no appreciable changes occurred in the bulk structure of the material.

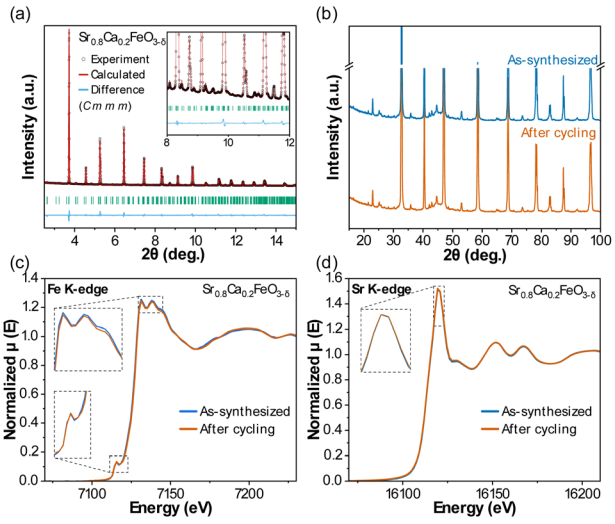

Fig. 4 XRD and XANES of $Sr_{0.8}Ca_{0.2}FeO_{3-\delta}$. (a) Full pattern refinement of the XRD pattern of $Sr_{0.8}Ca_{0.2}FeO_{3-\delta}$ (synchrotron XRD data, λ = 0.1770 Å); (b) XRD patterns of $Sr_{0.8}Ca_{0.2}FeO_{3-\delta}$ as-synthesized and after redox cycling (laboratory XRD data, Cu $K_{\alpha 1,2}$, λ = 1.5405 Å, λ = 1.5444 Å) zoomed in on the *y*-axis scale to highlight low-intensity peaks. XANES of $Sr_{0.8}Ca_{0.2}FeO_{3-\delta}$ as-synthesized and after redox cycling at the (c) Fe K-edge and (d) Sr K-edge.

To determine whether changes in the oxidation state and/or local structure of Fe or Sr in the perovskite occurred during redox cycling in the oxidized state (*i.e.* comparing the as-synthesized $Sr_{0.8}Ca_{0.2}FeO_{3-\delta}$ and the material after ten cycles), we applied X-ray absorption near edge structure (XANES) analysis of $Sr_{0.8}Ca_{0.2}FeO_{3-\delta}$ as a fingerprint technique. Note that these measurements were performed *ex situ*, and hence the samples were exposed to ambient conditions prior to the measurements. The Fe K-edge XANES in Fig. 4c shows features typical for a Fe-containing perovskite, with a white line at 7130 eV due to the dipole-allowed transitions from Fe 1s to 4p (with two additional peaks at 7132 eV and 7138 eV), and a pre-edge peak due to the quadrupolar transitions from Fe 1s to 3d at ~7115 eV, corresponding to a valence state of Fe between Fe^{3+} and Fe^{4+} (Fig. S8†).[58] The Sr K-edge XANES in Fig. 3d shows a sharp white line at ~16 112 eV, in line with previous XANES reports on Sr-based perovskite in the oxidized state and corresponding to a valence state of Sr^{2+}.[59] A comparison of the spectra collected for the as-synthesized and redox cycled materials confirms that the local structure of the perovskite did not change appreciably during redox cycling.

3.2.2 Reduction pathway. As XRD and XANES analysis, probing the bulk average and local structures, respectively, did not show changes of $Sr_{0.8}Ca_{0.2}FeO_{3-\delta}$ during redox cycling, we performed additional *in situ* XRD measurements (laboratory based) to probe the reduction pathway of $Sr_{0.8}Ca_{0.2}FeO_{3-\delta}$ and determine whether the reduction pathway changes with cycle number. Upon heating from room temperature to 500 °C in air, we observed a transition from an orthorhombic to a cubic perovskite structure, and also a shift of the peak positions to lower angles due to lattice expansion. The observed XRD pattern at 500 °C was refined by employing a cubic $Pm\bar{3}m$ space group, yielding the unit cell parameters $a = b = c = 3.897(1)$ Å (Fig. S9†). The evolution of the most relevant diffraction peaks in the 2θ range 31–33° was followed under redox conditions (500 °C, reduction in N_2 and oxidation in compressed air), and the XRD data collected in the reduction steps of the first, fifth and tenth cycle are plotted in Fig. 5a–c, respectively. The respective contour plots (intensity *vs.* time and 2θ angle) are shown in Fig. 5d–f. By inspecting the evolution of the intensity and the position of the peaks in each cycle, we identify three regions. (I) A transition within the perovskite phase in which the 2θ position of the cubic perovskite peak, indexed as (110), shifts towards lower angles due to lattice expansion, as iron was reduced and oxygen vacancies were generated within the perovskite lattice.[60] (II) The appearance of three new peaks due to the formation of a brownmillerite phase, with the general formula $ABO_{2.5}$ and an orthorhombic crystal structure (*Ibm*2), indexed as (020), (411) and (002).[14] The phase transition from perovskite to brownmillerite involves a decrease in the symmetry of the lattice and the ordering of oxygen vacancies.[57] In this second stage, there is also a simultaneous shift of the position of the perovskite peak (110) towards lower diffraction angles, but at a slower rate compared to region (I). (III) The presence of only the brownmillerite phase without any further notable structural changes with time, indicating that most of the oxygen had been released from the oxygen carrier.

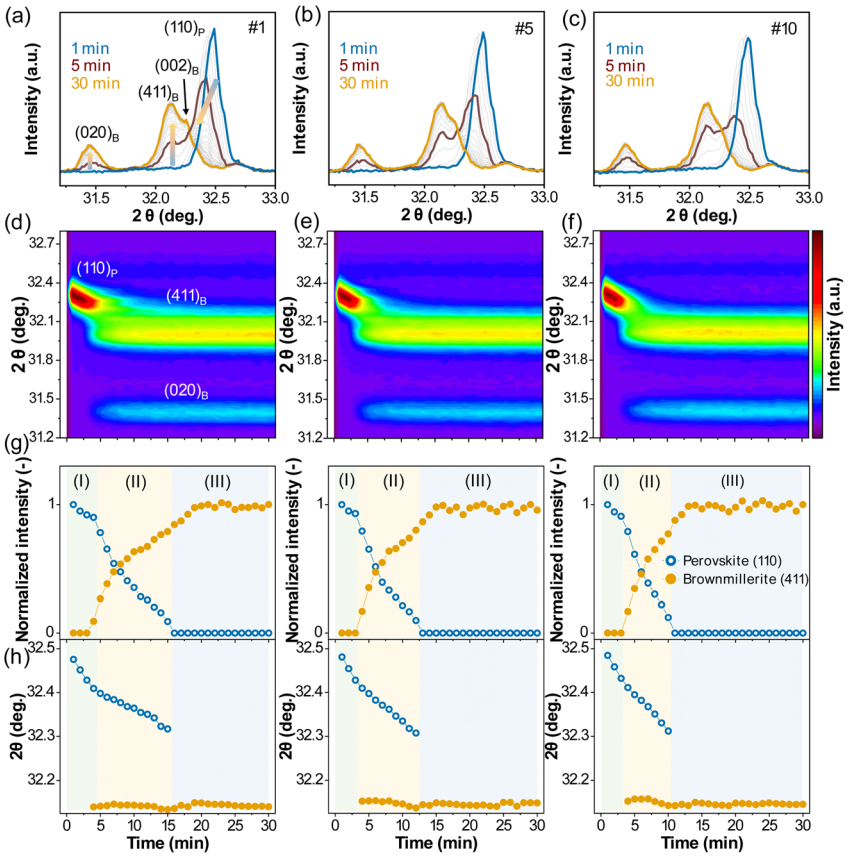

Fig. 5 *In situ* XRD measurements during redox cycling of $Sr_{0.8}Ca_{0.2}FeO_{3-\delta}$. The patterns were collected at 500 °C after switching from air to N_2; the acquisition time was ~65 seconds per pattern, and reported here at (a) and (d) first cycle, (b) and (e) fifth cycle and (c) and (f) tenth cycle. The (110) peak was assigned to a cubic perovskite phase, while the (020), (411) and (020) peaks belong to a brownmillerite phase. (g) Evolution of the integrated intensity normalized with respect to the maximum observed intensity and (h) peak position of the perovskite (110) and brownmillerite (411/002) peaks. The highlighted areas in light green, yellow and blue define the identified three regions (I), (II) and (III) of the phase transition from the perovskite to brownmillerite phase.

For a quantitative assessment of the phase transition during oxygen release, we fitted the observed peaks to analyze the evolution of their integrated intensities and positions. The integrated intensity of the peaks is proportional to the phase quantity, and the position of the peaks relates to the lattice parameters.[50] Fig. 5g and h show the results of the peak fitting for the first cycle, the fifth cycle and the tenth cycle. The evolution of the lattice parameter of the cubic perovskite phase, calculated based on the (110) peak position, is reported in Fig. S10.† Comparing the three representative cycles in Fig. 5g and h, the total duration of the phase transition from the perovskite to the brownmillerite phase during the reduction step (*i.e.* from $t = 0$ to the beginning of region (III)) decreased with cycle number (~15 min in the first cycle, ~12 min in the fifth cycle, and ~10 min in the tenth cycle). The decrease in the total reduction time points to an activation during cycling and is in line with the results of the TGA experiments (*e.g.* Fig. 1a). The duration of region (I) was between 3 and 4 min in cycles one, five and ten (Fig. 5g and h). Thus, within the time resolution of our laboratory base XRD (~65 s per scan), no appreciable changes of the duration of region (I) with cycle number were found. On the other hand, we observed a relevant change in the duration of region (II), which decreased with increasing cycle number (~11 min in the first cycle, ~8 min in the fifth cycle, and ~6 min in the tenth cycle). In region (II), the rate of the shift of the position of the perovskite peak and the phase transition from the perovskite to the brownmillerite phase increased with cycle number (Fig. S11†).

Subsequently, the structural evolution of the oxygen carrier as probed by *in situ* XRD was correlated with the amount of oxygen released through two separate sets of experiments: The reduction of the as-synthesized oxygen carrier in the TGA at 500 °C in N_2 was terminated at different times and the sample was cooled rapidly such that further oxygen release was prohibited (Fig. S12a†). The partially reduced oxygen carrier samples were then analyzed by XRD at room temperature (Fig. S12b and S12c†). Here, after only 1 min of reduction (point 2), when the oxygen released by the oxygen carrier was 0.32 wt%, the brownmillerite peaks were already visible. This indicates that the amount of oxygen released within region (I) (Fig. 5g and h) was relatively low (<0.3 wt%) and that most of the oxygen release occurred while the oxygen carrier transitioned from the perovskite to brownmillerite phase, *i.e.* in region (II). The XRD pattern of activated $Sr_{0.8}Ca_{0.2}FeO_{3-\delta}$ (treatment in synthetic air

for 2 h at 600 °C) after 1 min of reduction (point 2*, 0.42 wt% oxygen release) showed a larger fraction of the brownmillerite phase than point 2, confirming that the rate of phase evolution and oxygen release were directly correlated in region (II).

In the second set of experiments, we correlated the structural transition of $Sr_{0.8}Ca_{0.2}FeO_{3-\delta}$ from the perovskite to brownmillerite phase with pO_2 at 500 °C under equilibrium conditions (Fig. S13a†). From TGA measurements performed under identical conditions (*i.e.* 500 °C and varying ratios of N_2/air to obtain different pO_2, Fig. S13b†), we derived the maximum weight fraction of oxygen that can be released from the oxygen carrier without transitioning to the brownmillerite phase. As can be seen from Fig. S13a,† the brownmillerite phase is thermodynamically not favored for $pO_2 \geq 0.04$ bar at 500 °C. For $pO_2 = 0.04$ bar, Fig. S13b† indicates that maximal ~0.31 wt% of oxygen can be released from the oxygen carrier while avoiding the formation of a brownmillerite phase. Compared with $pO_2 = 0.21$ bar, the perovskite peak (110) shifted by 0.083° at $pO_2 = 0.04$ bar, corresponding to a change in the cell parameter of $\Delta a = 0.0108$ Å. This value is consistent with the evolution of the cell parameter during region (I), $\Delta a = 0.01012$ Å in Fig. S10,† and confirms that only a relatively small fraction of oxygen is released by $Sr_{0.8}Ca_{0.2}FeO_{3-\delta}$ at 500 °C before the transition to a brownmillerite occurs, and that the effect of activation of the oxygen carrier is most significant when the brownmillerite phase has been formed.

In summary, the analysis of the *in situ* XRD measurements showed a marked increase in the rate of phase transition during reduction (region (II)) upon cycling, consistent with the activation phenomenon observed in the TGA. We also observed that in each cycle the phase transition from the perovskite to brownmillerite phase was preceded by a reduction within the perovskite structure (region (I)), which occurred at a similar rate in all cycles (within the time resolution of the *in situ* XRD measurements that was ~65 s per scan, and possibly affected by the slow gas displacement in the reaction chamber when switching from air to N_2). The amount of oxygen released within region (I) was relatively small (~0.3 wt%) and the principal reaction pathway during reduction appeared to remain unchanged with cycling, as no other intermediate phases that might have contributed to the activation of the perovskite were observed within the narrow 2θ range investigated. We note that a full range XRD pattern with a higher time-resolution would be required (*e.g.* using synchrotron-based XRD) to confirm that no phases other than perovskite and brownmillerite are formed during oxygen release. The following section focuses on the analysis of possible changes in the surface area, pore volume and morphology of $Sr_{0.8}Ca_{0.2}FeO_{3-\delta}$ with cycle number since previous studies have argued that changes of these properties are the primary cause for the activation of oxygen carriers.[24–27]

3.3 Surface area, pore volume and morphology of $Sr_{0.8}Ca_{0.2}FeO_{3-\delta}$ before and after redox cycling

The morphology of the as-synthesized perovskite (sieved to 53–106 μm) and after ten redox cycles was studied through N_2 sorption. For the as-synthesized sample, the BET surface area and the total pore volume were 2 m^2 g^{-1} and 0.01 cm^3 g^{-1}, respectively; after ten redox cycles, these values did not change (*i.e.* 2 m^2 g^{-1} and 0.01 cm^3 g^{-1}, respectively). Equally, also the distributions of the pore volume, shown in Fig. S14a,† measured before and after cycling did not show significant differences. The morphology before and after redox cycling was also studied by means of HR-SEM measurements of dense pellets of $Sr_{0.8}Ca_{0.2}FeO_{3-\delta}$, Fig. S14b.† The images of the as-synthesized pellets before and after redox cycling show no discernable changes in the morphology, and we observed a very similar grain size before (55 ± 5 nm) and after cycling (57 ± 4 nm), assuming spherical grains and by averaging more than 20 grains before and after cycling.

Hence, the analysis of the textural properties of the sample, *i.e.* surface area, pore volume and morphology, did not show any significant changes over redox cycling that would explain the observed activation. Different from most other studies on oxygen carrier activation in chemical looping, relatively small particles were used in our investigation, such that morphological changes such as surface cracks might have been observed had larger particles (say, >500 μm) been used.

3.4 The role of the surface elemental composition in the oxygen exchange rate

XPS measurements were used to probe the elemental composition at and close to the surface of the following oxidized samples: as-synthesized, after a representative number of cycles (*viz.* after 1, 3, 5 or 10 redox cycles performed in the TGA at 500 °C), after exposure to 50% CO_2 at 500 °C in the TGA, and after activation without exposure to ambient air. In the latter case, the oxygen carrier was activated in a quartz tube reactor at 700 °C under N_2, then oxidized in synthetic air, followed by cooling to room temperature. The reactor was then flushed with N_2 and transferred to a glovebox, where the oxygen carrier sample was placed in a custom-made air-tight cell for the XPS measurement. Note that for the other samples the XPS data were collected within 24 h after the TGA measurement to mitigate changes to the sample due to CO_2 in ambient air (see Fig. 3a). When comparing the Sr 3d spectra with cycle number in Fig. 6a, a clear trend was observed, *i.e.* an increase in the shoulder feature at ~131.2 eV and a decrease in the intensity of the secondary peak at ~134.3 eV with cycle number; the features at 131.2 eV and 134.3 eV correspond to surface- and lattice-Sr, respectively.[39,46,48,61–63] Similarly, the O 1s spectra (Fig. 6b) showed a change in the distribution of oxygen species with cycle number, specifically, the intensity of the feature at ~528.8 eV (lattice oxygen[64,65]) increased with cycle number, while the intensity of the feature at ~531.3 eV (surface oxygen species[64–66]) decreased. Lastly, the C 1s spectra displayed two peaks at ~284.6 eV and at ~289.1 eV (Fig. 6c, note that we highlight only the region 287 to 291 eV); the first peak (not shown in Fig. 6c) was due to the C used for the calibration of the spectra, while the latter can be assigned to carbonate species on the surface of the sample.[64–67] We observed a reduced intensity of the peak at 289.1 eV due to carbonates with increasing cycle number, but the peak was still seen after ten redox cycles at 500 °C,

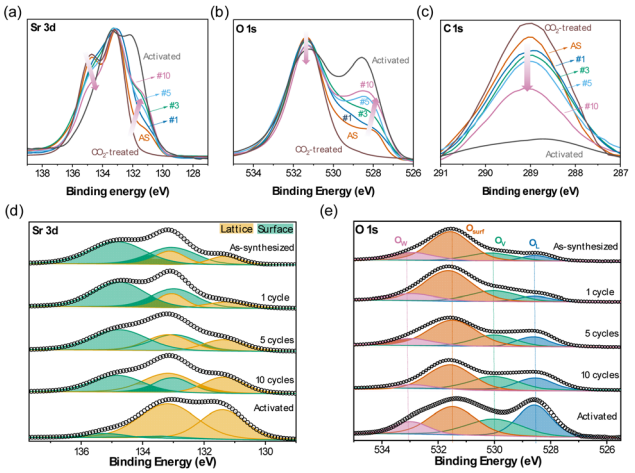

Fig. 6 XPS collected of as-synthesized, activated, CO_2-treated $Sr_{0.8}Ca_{0.2}FeO_{3-\delta}$ and after 1, 3, 5 and 10 redox cycles in the TGA. Evolution of the (a) Sr 3d, (b) O 1s and (c) C 1s spectra of $Sr_{0.8}Ca_{0.2}FeO_{3-\delta}$ upon redox cycling. Fittings of the (d) Sr 3d and (e) O 1s spectra of $Sr_{0.8}Ca_{0.2}FeO_{3-\delta}$. Note that the activated sample was prepared in a packed bed reactor containing quartz wool (SiO_2) that could not be separated entirely from the oxygen carrier prior to the XPS measurement. The apparent increase in the deconvolution peak O_W due to adsorbed water was in fact caused by the presence of SiO_2 that gives a signal at the binding energy 532.9 eV.

suggesting that not all carbonates were removed or that a small amount of CO_2 was adsorbed as carbonates on the sample during sample transfer to the sealed vial. For the activated sample that was not exposed to ambient air, there was no significant peak due to carbonates.

Next, we fitted the relevant XPS spectra to yield a more quantitative interpretation of the changes occurring during redox cycling. Fig. 6d shows the fittings of the Sr 3d spectra, for which two distinct binding environments of Sr were observed, *i.e.* a low-energy component at ~131.2 eV, referred to as lattice-Sr (Sr bound in the lattice of the perovskite structure), and a high-energy component at ~134.2 eV, referred to as surface-Sr, in line with previous works.[39,40] Surface-Sr comprises surface-bound Sr, *i.e.* secondary phases in the termination layer of the perovskite (*e.g.* SrO_x, carbonates, hydroxides).[39,46,48] In the as-synthesized sample, a large fraction (~70%) of the Sr signal was ascribed to the surface-Sr species. Upon activation, the ratio of low-to high-energy Sr changed: the amount of surface-Sr species (potentially SrO_x or carbonates as indicated by the C 1s spectra) decreased, while the amount of lattice-Sr (*e.g.* Sr in the bulk perovskite structure) increased; in the activated sample hardly any surface-Sr species were seen, suggesting also that the surface had less defects. A similar observation was made by Tripković *et al.* when studying the reversible activation/deactivation of $La_{0.6}Sr_{0.4}FeO_3$, used as an electrode material in solid oxide cells.[39] They noted that the deactivation of the sample was not due to a change in the absolute amount of Sr on the surface, but due to changes in the ratio of Sr in the perovskite structure (lattice-Sr) to strontium in secondary phases (surface-Sr). Specifically, it was also observed that the ratio lattice-Sr to surface Sr species increased due to Sr segregation upon thermal activation (1000 °C in air).

Turning to the fitting of the O 1s region (Fig. 6e), four types of oxygen where used for its convolution: lattice oxygen species (O_L) at ~528.8 eV, oxygen species located in the vicinity of oxygen vacancies (O_V) at ~530.3 eV, surface oxygen species (*e.g.* hydroxyl OH^- and/or carbonate CO_3^{2-}, O_{surf} or O_{carb}) at ~531.3 eV, and adsorbed water (O_w) at ~533 eV.[6,64–66] Upon redox cycling, the area below and the intensity of the deconvolution peak due to lattice oxygen species O_L increased, while the area below and the intensity of the deconvolution peak ascribed to surface oxygen species O_{surf} decreased (Fig. 6b and e). The area below and the intensity of the deconvolution peak ascribed to oxygen vacancies O_V remained unchanged. For the activated sample, the contribution of lattice oxygen was increased significantly.

The Fe XPS spectra displayed two main peaks, at ~711.1 eV and ~724.5 eV, corresponding to Fe $2p_{3/2}$ and Fe $2p_{1/2}$, respectively, and a minor satellite peak at ~716.2 eV. The peak at ~711.1 eV was deconvoluted in Fe^{2+} $2p_{3/2}$ (~710.1 eV) and Fe^{3+} $2p_{3/2}$ (~712.3 eV), and the peak at ~724.5 eV was deconvoluted in Fe^{2+} $2p_{1/2}$ (~723.8 eV) and Fe^{3+} $2p_{3/2}$ (~726.3 eV).[39,46] A change in the relative intensity of the peaks ascribed to Fe^{2+} and Fe^{3+} was observed upon redox cycling, with a decrease in the ratio Fe^{2+}/Fe^{3+} with cycle number (Fig. S15a†). A summary of the peak positions and intensity of the analyzed spectra is provided in Table S2.† Analysis of the elemental atomic composition of the region close to the surface by XPS (Fig. S15b†) shows an enrichment of Fe at the surface of the perovskite after ten redox cycles. It is noteworthy that the relative concentration of Fe at the surface of the perovskite remained largely unchanged in the first five cycles, and it increased only after ten cycles once the material was activated by a large degree. This observation suggests that the effect of activation, which is most significant in the first few redox cycles, is not linked to a change of the relative atomic concentration of Fe at the surface.

Yet, the decrease in both surface oxygen O_{surf} and surface-Sr species in combination with a decrease in intensity of carbonates (C 1s spectra) suggest a decrease in the extent of secondary Sr-phases (presumably carbonate species) on the surface of the perovskite upon redox cycling.

Further evidence for the removal of surface carbonates during activation is provided through temperature programmed desorption (TPD) experiments in which the gas released during the heating up of $Sr_{0.8}Ca_{0.2}FeO_{3-\delta}$ in He was measured by a mass spectrometer (MS) (Fig. 7a). We observed the presence of CO_2 (m/z 44) in the off-gas at temperatures $\geq$ 465 °C that most likely originates from the decomposition of surface carbonate species. The decomposition onset temperature of 465 °C explains why $Sr_{0.8}Ca_{0.2}FeO_{3-\delta}$ was not activated in the TGA experiment at 450 °C (Fig. S5a†).

The MS data also shows that oxygen release started at lower temperatures, *i.e.* at ~400 °C, consistent with our previous results.[14] The release of oxygen did not affect the onset of the decomposition of surface carbonate species, as shown in a second control experiment: When using 5% O_2/He instead of pure He in the TPD experiment (Fig. 7d), CO_2 was detected

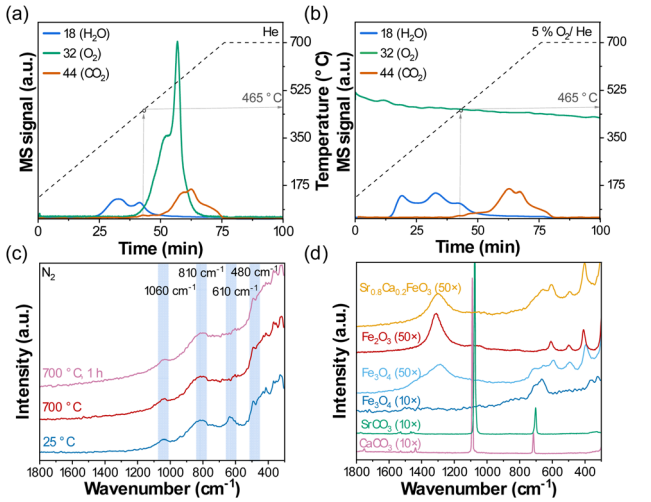

Fig. 7 Gas profiles collected with an MS at the outlet of the AutoChem during heating up to 700 °C in (a) He and (b) 5% O_2/He (*m*/*z* 18 was ascribed to H_2O, *m*/*z* 32 was ascribed to O_2, *m*/*z* 44 was ascribed to CO_2). (c) *In situ* Raman spectra of the as-synthesized $Sr_{0.8}Ca_{0.2}FeO_{3-\delta}$ heated up to 700 °C in N_2 and held for 1 h; (d) *ex situ* Raman spectra of reference materials, $CaCO_3$ (Sigma-Aldrich, >99.995%), $SrCO_3$ (Sigma-Aldrich, 99.9%), Fe_2O_3 (Sigma-Aldrich, >99%), Fe_3O_4 (Sigma-Aldrich, 95%) with 10× or 50× optical magnification, and of $Sr_{0.8}Ca_{0.2}FeO_3$ with 100× optical magnification.

again at around ~465 °C, while no oxygen was released by the perovskite because of the high pO_2. This result implies that the activation of the oxygen carrier, or the decomposition of the surface carbonate species, occurs also in a high pO_2 environment and not only under reducing conditions (*i.e.* in N_2 or He). This observation was confirmed through additional cycling experiments in the TGA at 500 °C, in which the sample was cycled once, then exposed to N_2, synthetic air (O_2/N_2) or compressed air (containing small quantities of CO_2) for 10 h, followed by another nine redox cycles (Fig. S6†). We observed that the material activated when exposed to both N_2 and O_2/N_2 for 10 h, such that the activation during the following redox cycles was less relevant when compared to Fig. 1. Note that the extent of activation was more significant during the treatment for 10 h in N_2 than in O_2/N_2. Only little activation was observed when using compressed air (contains ~400 ppm of CO_2), which emphasizes the detrimental impact of CO_2 even in low concentrations on the rate and extent of oxygen release.

Carbonate species (*e.g.* monodentate or bidentate carbonate, or bicarbonate) adsorbed to the surface of a material can also be probed using Raman spectroscopy.[67,68] Fig. 7c plots the results of an *in situ* Raman spectroscopy experiment when heating up $Sr_{0.8}Ca_{0.2}FeO_{3-\delta}$ to 700 °C in N_2 at 10 °C min^{-1}. The Raman spectra collected at 25 °C of the as-synthesized sample showed Raman bands at ~1060 cm^{-1}, ~810 cm^{-1}, ~610 cm^{-1} and ~480 cm^{-1}. At 700 °C, the bands at ~1060 cm^{-1} and ~480 cm^{-1} remained unchanged, while the band at ~610 cm^{-1} disappeared. The band at ~1060 cm^{-1} is similar to the strongest peak of the reference $SrCO_3$ (Fig. 7b; symmetric stretching vibration ν_1 (ref. 69)) but appears to be stable at 700 °C and thus is unlikely to contribute to the activation or deactivation of the perovskite that is taking place at much lower temperature. In fact, TGA measurements in Fig. S16† show that bulk $SrCO_3$ does not decompose below ~760 °C in N_2. Since the band at ~610 cm^{-1} disappeared when heating $Sr_{0.8}Ca_{0.2}FeO_{3-\delta}$ to 700 °C (Fig. 7c), it is unlikely that it originated from carbonate species as they have not been reported to give Raman bands in this region.[70] In Fig. 7d, Raman spectroscopy measurements of iron oxide references (Fe_3O_4 and Fe_2O_3 at room temperature) using a higher optical magnification (50× instead of 10×, which reduces the spot size of the laser to ~0.7 μm) indicate that the band at ~610 cm^{-1} (and also the one at ~480 cm^{-1}) originates from iron oxide. Indeed, the measurement of a magnified region of $Sr_{0.8}Ca_{0.2}FeO_{3-\delta}$ (50× at 25 °C, Fig. 7d and S17†) showed great similarity with Fe_2O_3, suggesting also that the oxygen carrier was initially not entirely composed of a single perovskite phase, but contained isolated clusters of iron oxide. Indeed, the data shown in Fig. S18† demonstrate that such iron oxide clusters disappeared after only one redox cycle, suggesting they were incorporated into the perovskite structure.[71] Upon exposure to CO_2 in the reaction cell at 500 °C, which led to a deactivation of the sample (Fig. 3), iron oxide clusters did not seem to reappear, confirming that the activation phenomenon is not linked to the presence and disappearance of small iron oxide clusters (Fig. S19†).

To summarize, the XPS and TPD measurements revealed the presence of surface carbonates on the as-synthesized materials that were effectively removed at temperatures > 475 °C, as also seen from the TGA results in Fig. 3c.

The formation of surface carbonate species was also reported by Yang *et al.* when studying $SrFe_{0.9}Ti_{0.1}O_{3-\delta}$ in the context of the electrochemical abatement of organic pollutants in water.

It was argued that the catalytic activity of the material decreased with increasing surface carbonate formation.[72] It was found that $SrCO_3$ formed when exposing $SrFe_{0.9}Ti_{0.1}O_{3-\delta}$ to pure CO_2 at T > 600 °C.[72] Furthermore, Østergaard *et al.* studied Ce-doped $SrFeO_3$ and observed a decrease in its catalytic activity due to the formation of "surface $SrCO_3$" when the sample was exposed to an aqueous environment, likely due to the presence of CO_2 in water.[73] Additionally, they demonstrated that the deactivation could effectively be reversed by a thermal treatment in air at 530 °C that removes $SrCO_3$. It is conceivable that the formed "surface" carbonate species (such as small clusters, highly defective or amorphous surface structures) require a lower temperature for decomposition than their "bulk" counterpart. This interpretation is supported by XRD measurements, as the formation of crystalline (bulk) carbonate species such as $SrCO_3$ was not observed. We also note that the presence of Ca in the oxygen carrier, which is known to readily form $CaCO_3$ in the presence of CO_2, did not influence the activation (or deactivation) behavior of the Sr-based oxygen carriers (see *e.g.* Fig. S2† in which the cyclic performances of different oxygen carrier compositions are compared). Hence, we speculate that the carbonates that are linked to material activation are strontium carbonate structures that originate from Sr segregation at the oxygen carrier's surface.[74] Such surface defects are known to reduce the rate of ionic transport

significantly, which may explain the lowered rate of oxygen transfer from the surface of the oxygen carrier to the bulk gas phase.[75,76] Raman spectroscopy measurements, however, were inconclusive in providing further insight on the nature of these carbonate structures, requiring further designated studies.

Importantly, our findings may explain why the activation phenomenon of Sr-based perovskites has been overlooked in other chemical looping studies, including theoretical works.[12,77] Often much higher operating temperatures were used ($T > 600$ °C[78–80]) such that the material activated already upon heating before the cycling experiment started,[81,82] and during the cycling experiment no stable surface carbonate species were formed. Further, when using high purity gases that do not contain CO_2 (laboratory experiments as opposed to practical industrial testing) such activation behavior would be absent.[83–86] From a practical point of view, it is exactly such CO_2 impurities in reducing and oxidizing gases that may be problematic when using Sr-based perovskites for chemical looping and other applications at low temperatures (*i.e.* ≤500 °C), because the rate of oxygen transfer to and from the perovskite (and therefore its practical OSC) is reduced substantially.

4. Conclusions

In this work, we provide fundamental material insight to explain the activation phenomenon (*i.e.* the increasing rate of oxygen release) of $Sr_{0.8}Ca_{0.2}FeO_{3-\delta}$-based oxygen carries upon redox cycling. To this end, we first carried out a systematic thermogravimetric analysis to study the influence of different operating conditions on the activation phenomenon (particle size, sample mass, flow rate, reducing gas, volume of the crucible) to exclude effects due to varying experimental conditions. An increase in the rate of oxygen release with redox cycling was observed at temperatures between 475 °C and 600 °C, and also for different perovskite compositions $Sr_{1-x}Ca_xFeO_{3-\delta}$ ($0 \leq x \leq 0.25$). From a structural point of view, XRD and XAS measurements did not show any apparent changes in the bulk (average or local) structure of the perovskite before and after activation. *In situ* XRD measurements showed that a significant increase in the rate of phase transition from perovskite to brownmillerite occurred upon activation. By combining TGA and *in situ* XRD measurements, we find that ~85% of the oxygen is released during the phase transition from perovskite to brownmillerite, which combines well the observed increase in the rate of phase transition and increase in rate of oxygen release with activation. From a textural point of view, no significant changes in surface area, pore volume and morphology of $Sr_{0.8}Ca_{0.2}FeO_{3-\delta}$ were observed when comparing the material before and after activation. Additionally, "aging" experiments revealed that the activation is only temporary, and that deactivation occurs upon exposure to CO_2 (but not H_2O), even in low concentrations contained in air (≪1%) and at ambient conditions.

XPS measurements combined with TPD measurements revealed the formation of surface carbonate species upon exposure to CO_2, which were abundant in the as-synthesized/deactivated sample, and likely originate from Sr segregation at the oxygen carrier's surface. Importantly, we show that such surface carbonate species are effectively removed upon treatment in a CO_2-free atmosphere above 465 °C.

Our experiments have shown that relatively low concentrations of CO_2 (≪1%) in the atmosphere lead to the formation of surface carbonate species that hinder the efficient oxygen transfer to and from the oxygen carrier, rendering the material almost impractical at the process level. Thus, means of CO_2 removal upstream of the chemical looping process would have to be implemented. It is therefore important for future research activities to investigate novel formulations or modifications of Sr-based oxygen carriers that can tolerate small quantities of CO_2 in the reducing and oxidizing gases.[75]

Author contributions

Giancarlo Luongo: data curation, formal analysis, validation, writing – original draft, Alexander H. Bork: conceptualization, writing – review & editing, Paula M. Abdala: conceptualization, writing – review & editing, Yi-Hsuan Wu: formal analysis, Evgenia Kountoupi: formal analysis, Felix Donat: conceptualization, writing – review & editing, funding acquisition, Christoph Müller: conceptualization, supervision, writing – review & editing, funding acquisition.

Conflicts of interest

There are no conflicts to declare.

Acknowledgements

The authors would like to acknowledge the Swiss Office of Energy (BFE, SI/501590-01) for financial support. This publication was created as part of NCCR Catalysis (grant number 180544), a National Centre of Competence in Research funded by the Swiss National Science Foundation. We acknowledge Swiss Federal Laboratories for Materials Science and Technology (EMPA) for access to the XPS facility. Dr Agnieszka Kierzkowska (ETH Zürich) is acknowledged for assisting with the SEM measurements. The SNBL and ESRF are acknowledged for the provision of beamtime and Drs Wouter van Beek, Dragos Stoian, and Agnieszka Paul-Poulain for assistance during XAS and XRD measurements. Angelo Bellia and Maximilian Krödel, Dr Denis Kuznetsov, Annelies Landuyt, David Niedbalka, and Alexander Oing are acknowledged for their support in the BET measurements, XPS analysis, microscopy measurements, TPD measurements, and discussions, respectively.

References

1 M. B. Hanif, M. Motola, S. Rauf, C. J. Li and C. X. Li, *Chem. Eng. J.*, 2022, **428**, 132603.
2 X. Mao, Z. Li, M. Li, X. Xu, C. Yan, Z. Zhu and A. Du, *J. Am. Chem. Soc.*, 2021, **143**(25), 9507–9514.
3 X. Zhu, Q. Imtiaz, F. Donat, C. R. Müller and F. Li, *Energy Environ. Sci.*, 2020, **13**, 772–804.

4 Y. Gao, X. Wang, J. Liu, C. Huang, K. Zhao, Z. Zhao, X. Wang and F. Li, *Sci. Adv.*, 2020, **6**(17), 9339.
5 Y. Zhu, D. Liu, H. Jing, F. Zhang, X. Zhang, S. Hu, L. Zhang, J. Wang, L. Zhang, W. Zhang and B. Pang, *Sci. Adv.*, 2022, **8**(15), 4072.
6 C. Sun, J. A. Alonso and J. Bian, *Adv. Energy Mater.*, 2021, **11**(2), 2000459.
7 Z. Wang, H. Huang, G. Li, X. Yan, Z. Yu, K. Wang and Y. Wu, *Appl. Phys. Rev.*, 2021, **8**(2), 021320.
8 H. Chen, M. Zhang, T. Tran-Phu, R. Bo, L. Shi, I. Di Bernardo, J. Bing, J. Pan, S. Singh, J. Lipton-Duffin and T. Wu, *Adv. Funct. Mater.*, 2021, **31**(4), 2008245.
9 X. Zhu, K. Li, L. Neal and F. Li, *ACS Catal.*, 2018, **8**(9), 8213–8236.
10 G. Luongo, F. Donat, A. H. Bork, E. Willinger, A. Landuyt and C. R. Müller, *Adv. Energy Mater.*, 2022, 2200405.
11 B. Bulfin, J. Vieten, D. E. Starr, A. Azarpira, C. Zachäus, M. Hävecker, K. Skorupska, M. Schmücker, M. Roeb and C. Sattler, *J. Mater. Chem. A*, 2017, **5**(17), 7912–7919.
12 J. Vieten, B. Bulfin, P. Huck, M. Horton, D. Guban, L. Zhu, Y. Lu, K. A. Persson, M. Roeb and C. Sattler, *Energy Environ. Sci.*, 2019, **12**(4), 1369–1384.
13 M. Kubicek, A. H. Bork and J. L. Rupp, *J. Mater. Chem. A*, 2017, **5**(24), 11983–12000.
14 G. Luongo, F. Donat and C. R. Müller, *Phys. Chem. Chem. Phys.*, 2020, **22**(17), 9272–9282.
15 D. Hosseini, F. Donat, S. M. Kim, L. Bernard, A. M. Kierzkowska and C. R. Müller, *ACS Appl. Energy Mater.*, 2018, **1**(3), 1294–1303.
16 J. Chen, L. Duan, F. Donat, C. R. Mueller, E. J. Anthony and M. Fan, *Chem. Eng. J.*, 2018, **351**, 1038–1046.
17 J. Ma, X. Tian, H. Zhao, S. Bhattacharya, S. Rajendran and C. Zheng, *Energy Fuels*, 2017, **31**(2), 1896–1903.
18 L. Chen, G. Wei and K. Liu, *Fuel Process. Technol.*, 2022, **228**, 107139.
19 A. Abad, J. Adanez, A. Cuadrat, F. Garcia-Labiano, P. Gayan and F. Luis, *Chem. Eng. Sci.*, 2011, **66**(4), 689–702.
20 T. Mattisson, S. Sundqvist, P. Moldenhauer, H. Leion and A. Lyngfelt, *Int. J. Greenhouse Gas Control*, 2019, **87**, 238–245.
21 H. Leion, T. Mattisson and A. Lyngfelt, *Int. J. Greenhouse Gas Control*, 2008, **2**(2), 180–193.
22 M. Johansson, T. Mattisson and A. Lyngfelt, *Ind. Eng. Chem. Res.*, 2004, **43**(22), 6978–6987.
23 D. Yamaguchi, L. Tang and K. Chiang, *Chem. Eng. J.*, 2017, **322**, 632–645.
24 G. L. Schwebel, H. Leion and W. Krumm, *Chem. Eng. Res. Des.*, 2012, **90**(9), 1351–1360.
25 Z. Yu, Y. Yang, S. Yang, Q. Zhang, J. Zhao, Y. Fang, X. Hao and G. Guan, *Carbon Resour. Convers.*, 2019, **2**(1), 23–34.
26 J. Adánez, A. Cuadrat, A. Abad, P. Gayán, L. F. de Diego and F. Garcia-Labiano, *Energy Fuels*, 2010, **24**(2), 1402–1413.
27 A. Cuadrat, A. Abad, J. Adánez, L. F. De Diego, F. García-Labiano and P. Gayán, *Fuel Process. Technol.*, 2012, **94**(1), 101–112.
28 P. Knutsson and C. Linderholm, *Appl. Energy*, 2015, **157**, 368–373.
29 L. Chen, J. Bao, L. Kong, M. Combs, H. S. Nikolic, Z. Fan and K. Liu, *Appl. Energy*, 2017, **197**, 40–51.
30 J. Bao, Z. Li, H. Sun and N. Cai, *Ind. Eng. Chem. Res.*, 2013, **52**(42), 14817–14827.
31 J. Bao, Z. Li and N. Cai, *Ind. Eng. Chem. Res.*, 2013, **52**(18), 6119–6128.
32 Y. Ku, H. C. Wu, P. C. Chiu, Y. H. Tseng and Y. L. Kuo, *Appl. Energy*, 2014, **113**, 1909–1915.
33 N. Khakpoor, E. Mostafavi, N. Mahinpey and H. De la Hoz Siegler, *Energy*, 2019, **169**, 329–337.
34 W. C. Cho, C. G. Kim, S. U. Jeong, C. S. Park, K. S. Kang, D. Y. Lee and S. D. Kim, *Ind. Eng. Chem. Res.*, 2015, **54**(12), 3091–3100.
35 Z. Ma, S. Zhang and Y. Lu, *Energy Fuels*, 2020, **34**(12), 16350–16355.
36 Z. Ma, S. Zhang and R. Xiao, *Energy Convers. Manage.*, 2019, **188**, 429–437.
37 Z. Ma, R. Xiao and L. Chen, *Energy Convers. Manage.*, 2018, **168**, 288–295.
38 Y. Saito, F. Kosaka, N. Kikuchi, H. Hatano and J. Otomo, *Ind. Eng. Chem. Res.*, 2018, **57**(16), 5529–5538.
39 Đ. Tripković, J. Wang, R. Küngas, M. B. Mogensen, B. Yildiz and P. V. Hendriksen, *Chem. Mater.*, 2022, **34**(4), 1722–1736.
40 Đ. Tripkovic, R. Küngas, M. B. Mogensen and P. V. Hendriksen, *J. Mater. Chem. A*, 2019, **7**, 11782–11791.
41 J. Suntivich, H. A. Gasteiger, N. Yabuuchi, H. Nakanishi, J. B. Goodenough and Y. Shao-Horn, *Nat. Chem.*, 2011, **3**, 546–550.
42 N. Tsvetkov, Q. Lu, L. Sun, E. J. Crumlin and B. Yildiz, *Nat. Mater.*, 2016, **15**, 1010–1016.
43 Y. Chen, W. Jung, Z. Cai, J. J. Kim, H. L. Tuller and B. Yildiz, *Energy Environ. Sci.*, 2012, **5**, 7979–7988.
44 M. Kubicek, G. M. Rupp, S. Huber, A. Penn, A. K. Opitz, J. Bernardi, M. Stöger-Pollach, H. Hutter and J. Fleig, *Phys. Chem. Chem. Phys.*, 2014, **16**(6), 2715–2726.
45 W. Lee, J. W. Han, Y. Chen, Z. Cai and B. Yildiz, *J. Am. Chem. Soc.*, 2013, **135**, 7909–7925.
46 Z. Cai, M. Kubicek, J. Fleig and B. Yildiz, *Chem. Mater.*, 2012, **24**, 1116–1127.
47 G. M. Rupp, A. K. Opitz, A. Nenning, A. Limbeck and J. Fleig, *Nat. Mater.*, 2017, **16**, 640–645.
48 D. Kim, R. Bliem, F. Hess, J.-J. Gallet and B. Yildiz, *J. Am. Chem. Soc.*, 2020, **142**, 3548–3563.
49 J. Rodríguez-Carvajal and T. Roisne, *International Union for Crystallography*, Newletter N, vol. 20, 1998.
50 B. D. Cullity, *Elements of X-ray Diffraction*, Addison-Wesley Publishing, 1956.
51 D. A. Shirley, *Phys. Rev. B: Solid State*, 1972, **5**(12), 4709.
52 J. H. Scofield, *J. Electron Spectrosc. Relat. Phenom.*, 1976, **8**(2), 129–137.
53 B. Ravel and M. Newville, *J. Synchrotron Radiat.*, 2005, **12**, 537–554.
54 I. A. Starkov, S. F. Bychkov, S. A. Chizhik and A. P. Nemudry, *Chem. Mater.*, 2014, **26**(6), 2113–2120.
55 E. J. Popczun, S. Natesakhawat, C. M. Marin, T. D. Nguyen-Phan, Y. Zhou, D. Alfonso and J. W. Lekse, *J. Mater. Chem. A*, 2020, **8**(5), 2602–2612.

56 J. Dou, E. Krzystowczyk, X. Wang, A. R. Richard, T. Robbins and F. Li, *J. Phys.: Energy*, 2020, **2**(2), 25007.
57 J. P. Hodges, S. Short, J. D. Jorgensen, X. Xiong, B. Dabrowski, S. M. Mini and C. W. Kimball, *J. Solid State Chem.*, 2000, **151**(2), 190–209.
58 O. Haas, U. F. Vogt, C. Soltmann, A. Braun, W. S. Yoon, X. Q. Yang and T. Graule, *Mater. Res. Bull.*, 2009, **44**(6), 1397–1404.
59 K. Tamai, S. Hosokawa, K. Kato, H. Asakura, K. Teramura and T. Tanaka, *Phys. Chem. Chem. Phys.*, 2020, **22**(42), 24181–24190.
60 D. D. Taylor, N. J. Schreiber, B. D. Levitas, W. Xu, P. S. Whitfield and E. E. Rodriguez, *Chem. Mater.*, 2016, **28**(11), 3951–3960.
61 E. J. Crumlin, E. Mutoro, Z. Liu, M. E. Grass, M. D. Biegalski, Y. L. Lee, D. Morgan, H. M. Christen, H. Bluhm and Y. Shao-Horn, *Energy Environ. Sci.*, 2012, **5**(3), 6081–6088.
62 E. J. Crumlin, E. Mutoro, W. T. Hong, M. D. Biegalski, H. M. Christen, Z. Liu, H. Bluhm and Y. Shao-Horn, *J. Phys. Chem. C*, 2013, **117**(31), 16087–16094.
63 Y. Li, W. Zhang, T. Wu, Y. Zheng, J. Chen, B. Yu, J. Zhu and M. Liu, *Adv. Energy Mater.*, 2018, **8**(29), 1801893.
64 Y. Gao, X. Wang, J. Liu, C. Huang, K. Zhao, Z. Zhao and F. Li, *Sci. Adv.*, 2020, **6**(17), 1597–1617.
65 D. Chen, D. He, J. Lu, L. Zhong, F. Liu, J. Liu, J. Yu, G. Wan, S. He and Y. Luo, *Appl. Catal., B*, 2017, **218**, 249–259.
66 S. Song, W. Xu, J. Zheng, L. Luo, M. H. Engelhard, M. E. Bowden, B. Liu, C. M. Wang and J. G. Zhang, *Nano Lett.*, 2017, **17**(3), 1417–1424.
67 H. An, L. Wu, L. D. Mandemaker, S. Yang, J. de Ruiter, J. H. Wijten, J. C. Janssens, T. Hartman, W. van der Stam and B. M. Weckhuysen, *Angew. Chem., Int. Ed.*, 2021, **60**(30), 16576–16584.
68 Y. Dai, M. Xu, Q. Wang, R. Huang, Y. Jin, B. Bian, C. Tumurbaatar, B. Ishtsog, T. Bold and Y. Yang, *Appl. Catal., B*, 2020, **277**, 119271.
69 W. Kaabar, S. Bott and R. Devonshire, *Spectrochim. Acta, Part A*, 2011, **78**(1), 136–141.
70 G. Socrates, *Infrared and Raman Characteristic Group Frequencies: Tables and Charts*, John Wiley & Sons, 2004.
71 Y. Yang, Y. Li, Y. Jiang, M. Zheng, T. Hong, X. Wu and C. Xia, *Electrochim. Acta*, 2018, **284**, 159–167.
72 F. Donat and C. R. Müller, *Appl. Catal., B*, 2020, **278**, 119328.
73 M. B. Østergaard, A. B. Strunck, V. Boffa and M. K. Jørgensen, *Catalysts*, 2022, **12**(3), 265.
74 M. T. Dunstan, F. Donat, A. H. Bork, C. P. Grey and C. R. Müller, *Chem. Rev.*, 2021, **121**(20), 12681–12745.
75 B. Koo, K. Kim, J. K. Kim, H. Kwon, J. W. Han and W. Jung, *Joule*, 2018, **2**(8), 1476–1499.
76 J. Irvine, J. L. Rupp, G. Liu, X. Xu, S. Haile, X. Qian, A. Snyder, R. Freer, D. Ekren, S. Skinner and O. Celikbilek, *J. Phys.: Energy*, 2021, **3**(3), 031502.
77 X. Wang, Y. Gao, E. Krzystowczyk, S. Iftikhar, J. Dou, R. Cai, H. Wang, C. Ruan, S. Ye and F. Li, *Energy Environ. Sci.*, 2022, **15**(4), 1512–1528.
78 Z. Rui, J. Ding, Y. Li and Y. S. Lin, *Fuel*, 2010, **89**(7), 1429–1434.
79 Q. Yin, J. Kniep and Y. S. Lin, *Chem. Eng. Sci.*, 2008, **63**(8), 2211–2218.
80 R. Cai, J. Dou, E. Krzystowczyk, A. Richard and F. Li, *Chem. Eng. J.*, 2022, **429**, 132370.
81 X. Wang, E. Krzystowczyk, J. Dou and F. Li, *Chem. Mater.*, 2021, **33**(7), 2446–2456.
82 E. J. Popczun, T. Jia, S. Natesakhawat, W. Xu, C. M. Marin, Y. Duan and J. W. Lekse, *J. Alloys Compd.*, 2022, **896**, 162783.
83 H. Ikeda, A. Tsuchida, J. Morita and N. Miura, *Ind. Eng. Chem. Res.*, 2016, **55**(22), 6501–6505.
84 T. Masunaga, J. Izumi and N. Miura, *J. Ceram. Soc. Jpn.*, 2010, **118**(1382), 952–954.
85 G. E. Wilson, I. D. Seymour, A. Cavallaro, S. J. Skinner and A. Aguadero, *J. Electrochem. Soc.*, 2022, **169**(4), 044509.
86 Y. Yoshiyama, S. Hosokawa, H. Asakura, K. Teramura and T. Tanaka, *J. Phys. Chem. C*, 2022, **126**(9), 4415–4422.

